Deterministic deposition of nano-particles with sub 10 nm resolution.

Stefan Fringes, C. Schwemmer, Colin D. Rawlings, and Armin W. Knoll*

IBM Research Zurich, Säumerstrasse 4, 8803 Rüschlikon, Switzerland

E-mail: ark@zurich.ibm.com

Phone: +41 (0)44 7248246

Overall device design and Brownian transport to the compartment

All experiments were done in the nanofluidic confinement apparatus described previously in detail.[1,2] It provides a platform to align a glass surface with respect to a sample with a precision of $\approx$ 1 nm / 10 μm. Moreover, the gap between the surfaces can be tuned with nanometer precision down to direct contact. Interference of laser light used for illumination provides the basis for a precise measurement of the gap distance and therefore also of the parallel alignment.[1] In order to reach very small gaps a pillar of $\approx 30\mu$m height and $\approx 100\mu$m width is fabricated in the center of the cover-glass by wet-etching. 25 nm thick gold electrodes are deposited next to the pillar by shadow evaporation in order to provide a force for the particles. A sketch of the system is shown in Figure 1(a). All surfaces in the system, that is of the glass, the polymer, and the particles, are negatively charged in our system. As previously investigated in detail,[3] the main transduction mechanism of the electric field onto the particle force is via an electroosmotic plug flow in the nanofluidic slit resulting in a force

on the particles towards the negatively charged electrodes. This force is used to provide a zero mean AC force for the Brownian motor operation.[3]

Figure 1 (b) shows the written and imaged topography of a PPA film, which we used to arrange 60 nm gold spheres to form the letters IBM. The reservoir areas (inside the blue boxes) were patterned $\approx$ 75 nm deep into a polymer film and were capable of trapping particles at a gap distance between the cover-glass and the unpatterned polymer surface of $\approx$ 160 nm, while the diffusivity of particles outside the patterned region was still $\approx 4\,\mu\mathrm{m}^2/\mathrm{s}$ in one dimension. Nevertheless, the electrical double layer repulsion prevented particles from entering the confined space between the glass-mesa and the polymer surface. While dwelling at this separation for a few minutes, all particles which were confined below the glass mesa either diffused out of the slit or were concentrated in the reservoirs as shown by the five diffusing particles marked by the green circles in Figure 2 (a).

The assembly site is inside the red box in Figure 1 (a). A magnified and rescaled image of the topography of this region is shown in Figure 1 (b). The average depth of the assembly site is recessed by $\approx$ 22 nm as indicated by the dashed black line and the red profile in Figure 1 (d). Inside this box 35 traps form the letters IBM. The targeted positions of these traps are at the intersection points of a 200 nm spaced grid and their additional depth is $\geq$ 10 nm. The sketch in Figure 1 (c) illustrates the confinement dependent topographical trapping. The gap distance d_{IBM} between the cover-glass and the recessed PPA surface in the assembly site is used to characterize the confinement dependent trapping behavior.

In order to deliver the particles from the deeper written reservoirs to the shallower assembly site, the Brownian ratchets inside the green box in Figure 1 (a) were used. The ratchets allowed gradually moving the particles from the reservoir, where the repulsive interaction was low, to the assembly site, which had a higher repulsive interaction potential. Effective transport was guaranteed by the design of the ratchet amplitude, which became constantly smaller with increasing offset as depicted by the green line in Figure 1 (d). In order to actually operate the ratchet i.e., to bring the system out of equilibrium, a 50 Hz square wave

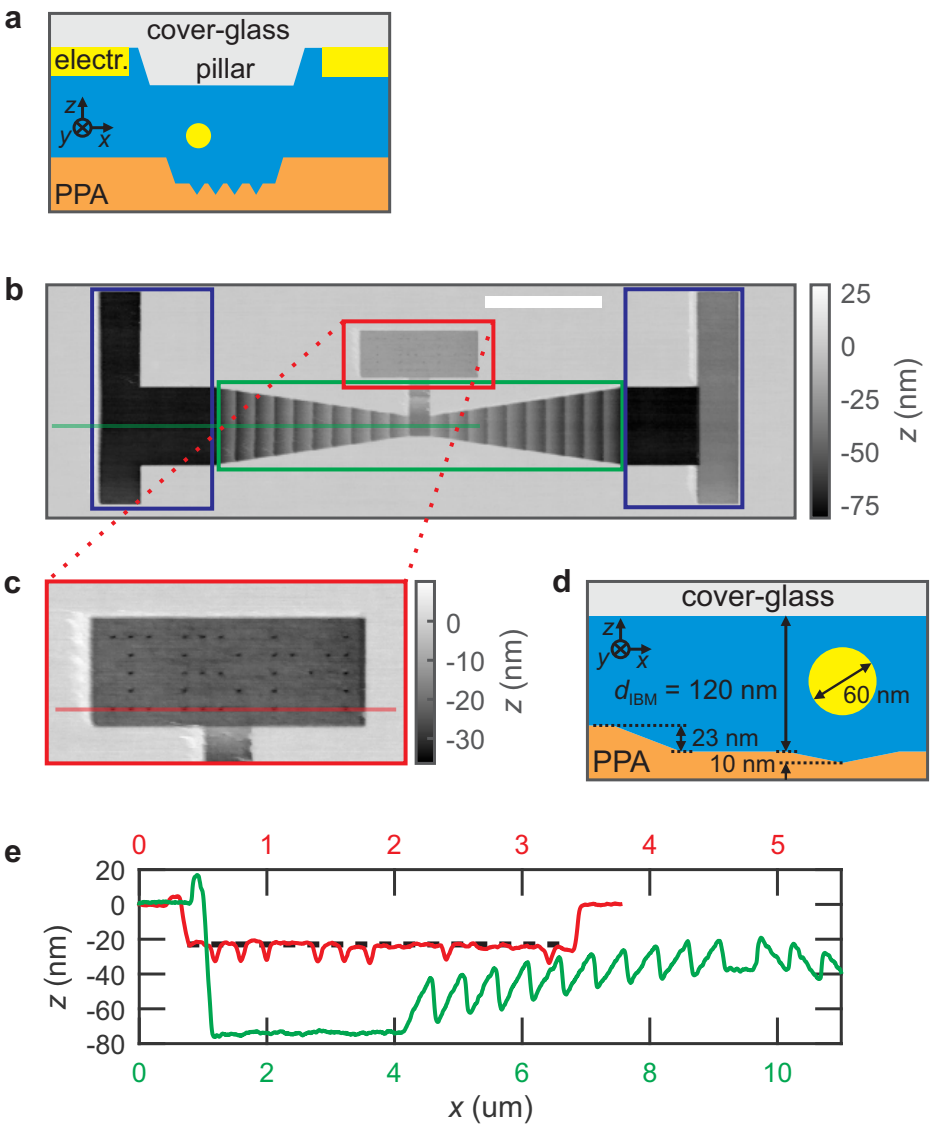

Figure 1: (a) Schematics of the nanofluidic slit. The nanofluidic confinement is provided by a glass pillar ($\approx$ 100μm wide and $\approx$ 30μm high, etched into a cover-glass) and the patterned polyphthalaldehyde (PPA) polymer film. At the side of the pillar gold electrodes are deposited at a distance of 1.2 mm onto the cover-glass. These electrodes are used to provide a particle force via electroosmotic force-transduction.[3] (b)The topography of the overall device was imaged and patterned by tSPL. The aim of the recessed areas inside the blue boxes is to trap nanospheres at a larger gap distance. The particles are then transported by the ratchets inside the green box to the assembly site, which is marked by the red box. (b) The assembly site has a depth of $\approx$ 22 nm with 35 traps. The traps are recessed by another $\approx$ 10 nm and form the letters IBM. The scale bar is 3 μm. (c) A true to scale sketch of a 60 nm Au sphere, which is trapped in a 10 nm deep conical recess at a glass-PPA separation next to the trap of $d_{\mathrm{IBM}} = 120$ nm. (d) Cross-sectional profile along the green and red lines shown in (a) and (b), respectively.

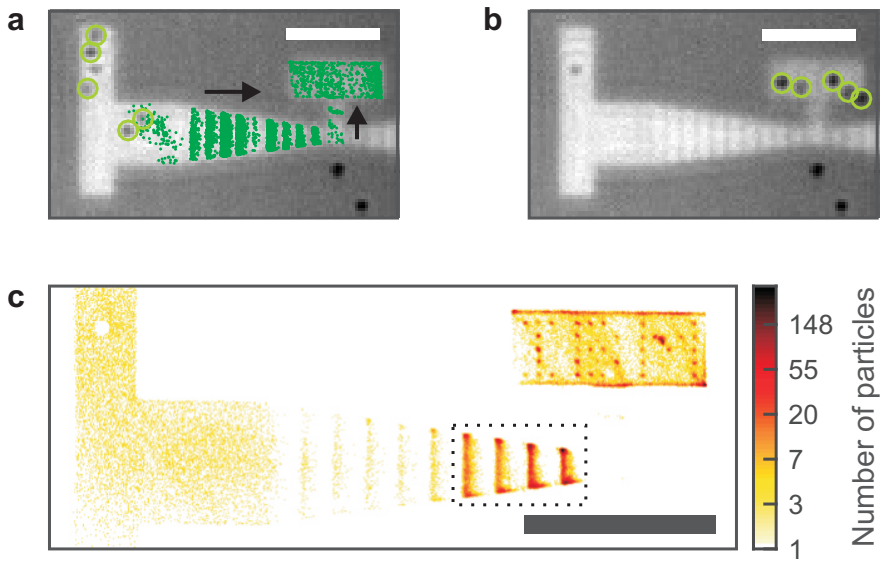

Figure 2: Transport of 60 nm spheres to the assembly site. (a) Five diffusive particles, marked by green circles, are trapped in the reservoir at a constant gap distance between the cover-glass and the unpatterned PPA surface of ≈ 112 nm. The unmarked particles are attached to the polymer surface. The green dots indicate measured particle locations of one particle, while applying a 50 Hz square wave potential of $|V| = 6$ V, which leads to directed motion in the direction of the black arrows. (b) The five mobile particles are concentrated at the assembly site. (c) The "heatmap" shows how often a 20 nm grid field is sampled by a particle during transport to the assembly site. (a-c) The scale bar is 3 μm.

potential of $|V| = 6\,\mathrm{V}$ was applied. This led to directed particle transport as indicated by the green dots in Figure 2 (a). While the confinement between the cover-glass and the unpatterned PPA surface was kept at a separation of $112.2 \pm 0.5\,\mathrm{nm}$ all mobile particles were transported to the assembly site as shown in Figure 2 (b).

The particle distribution for the entire transport is illustrated in Figure 2 (c). The so called "heatmap" counts the number of detected particles within a 20 nm grid field. Inside the black dotted box are the parts of the ratchet, which were sampled by the particles the most, which also means that they resided there the longest. The efficiency in a future experiment could be further improved, by either reducing the amplitude of the last ratchet teeth, or by increasing the amplitude of the other teeth and operating the ratchet at a larger gap distance or stronger forcing.

Correction of motion blur and noise

The measurements of the trapping energy and stiffness (see Fig. 2(g) of the main manuscript) are affected by the motion blur of the particles, due to the finite particle illumination time.[4] In the following paragraph we will present a method how this effect can be taken into account: The variance of positions σ_r^2, of a particle undergoing Brownian motion in such a parabolic potential, can be determined due to the equipartition theorem as[4]

$$\sigma_r^2 = \frac{k_B T}{k_r}. \tag{1}$$

For a direct measurement of the instantaneous particle positions the illumination time of the particles τ_{illu} has to be much smaller than their relaxation time

$$\tau_{\mathrm{rel}} = \gamma / k_r, \tag{2}$$

where $\gamma = 3\pi\eta a$ is the drag coefficient for a sphere of diameter a in a solution of viscosity $\eta = 1\,\mathrm{mPa\,s}$. For larger illumination times an averaged blurred position is detected, which leads to a narrower particle distribution and thus smaller measured variance $\sigma^2_{r,\,\mathrm{meas}} \leq \sigma^2_r$. The experimentally detected particles are illuminated by raster scanning a field of $\approx 40 \times 40\,\mu\mathrm{m}^2$ once with a $2\,\mu$m wide Gaussian beam within an exposure time of $\tau_{exp} = 1\,\mathrm{ms}$ and a line duration of $10\,\mu\mathrm{s}$. For the resulting laser line spacing of 400 nm we estimate that the particle is illuminated for five consecutive scan lines, since it is practically static for this time duration. Thus we estimate a particle illumination time of $\tau_{\mathrm{illu}} \lesssim 50\,\mu\mathrm{s}$. A motion blur and detection noise corrected measurement of the particle variance σ^2_r can be obtained by[4]

$$\sigma^2_r = \left(\sigma^2_{r,\,\mathrm{meas}} - \sigma^2_{r,\,\mathrm{noise}}\right) / \left(\frac{2}{\tau_{\mathrm{illu}}/\tau_{\mathrm{rel}}} - \frac{2}{\left(\tau_{\mathrm{illu}}/\tau_{\mathrm{rel}}\right)^2}\left(1 - e^{-\tau_{\mathrm{illu}}/\tau_{\mathrm{rel}}}\right)\right), \tag{3}$$

where $\sigma^2_{r,\,\mathrm{meas}}$ and $\sigma^2_{r,\,\mathrm{noise}}$ are the variance of particle positions without correction and caused by detection noise, respectively.

With the Equations (1) – (3) we can make a first estimation of the motion blurred relaxation time and thus calculate an updated variance of particle positions. Then we can re-calculate the trapping stiffness and the relaxation time. We iteratively optimize the variance of particle positions σ^2_r, the radial trapping stiffness k_r and the relaxation time τ_{rel}. After a few iterations the values saturate to the motion blur and detection noise corrected values. For the noise correction a standard deviation of $\sigma_{r,\,\mathrm{noise}} \approx 2.5\,\mathrm{nm}$ was used. This value is measured for immobilized particles as depicted by the black dashed line in Figure 2(f) of the main text.

The motion blur and detection noise corrected free energies are shown by the darker colors in Figure 3. In order to clarify the energy a particle gains when it is trapped, we have shifted all energies such that the average energy outside of the area of influence ($r > 90\,\mathrm{nm}$) is zero. The "blur- and noise-free" values for the trapping energy $F(0)$, the standard deviation of particle positions σ_r, the trapping stiffness k_r and the relaxation time τ_{rel} are shown for both

Table 1: The "blur- and noise-free" values for the trapping energy $F(0)$, the standard deviation of particle positions σ_r, the trapping stiffness k_r and the relaxation time τ_{rel}. The electrostatic interaction energy for a sphere with a surface potential $\psi_{S,0} = -58\,\mathrm{mV}$ confined by two parallel plates with surface potential $\psi_{P,0} = -67\,\mathrm{mV}$ can be calculated by Equation 4. ΔW_{edl} is the difference in energy between two such systems, where system 1 has a gap distance of d_{IBM} and system 2 has $d_{\mathrm{IBM}} + 10\,\mathrm{nm}$.

d_{IBM}	$120.2\,\mathrm{nm}$	$105.1\,\mathrm{nm}$
$F(0)$	$(-3.1 \pm 0.2)\,k_BT$	$(-6.7 \pm 0.4)\,k_BT$
ΔW_{edl}	$-3.8\,k_BT$	$-6.9\,k_BT$
σ_r	$(24.3 \pm 1.4)\,\mathrm{nm}$	$(17.0 \pm 1.1)\,\mathrm{nm}$
k_r	$(6.9 \pm 0.4)\,\mathrm{fN/nm}$	$(14.2 \pm 0.9)\,\mathrm{fN/nm}$
τ_{rel}	$(81 \pm 5)\,\mu\mathrm{s}$	$(40 \pm 3)\,\mu\mathrm{s}$

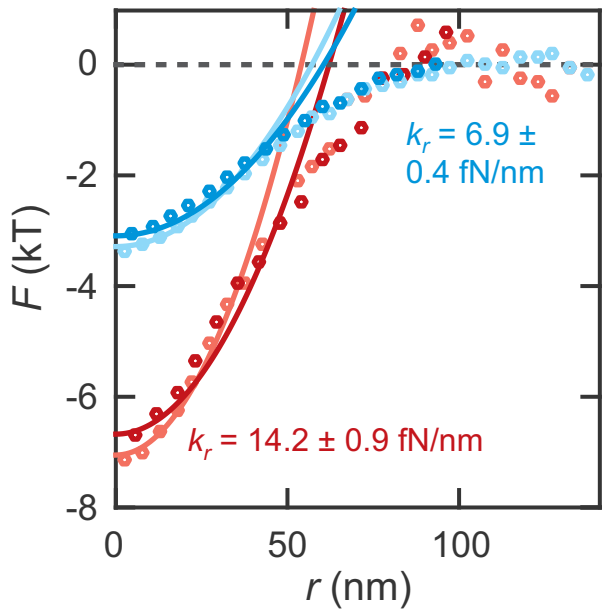

Figure 3: Radial free energies $F(r)$ averaged over the particle and trap ensemble at a gap distance of $d_{\mathrm{IBM}} \approx 120.2\,\mathrm{nm}$ (blue) and $d_{\mathrm{IBM}} \approx 105.1\,\mathrm{nm}$ (red). The brighter circles are determined via the Boltzmann relation $F(r) = -k_BT \ln P(r)$ using the measured empirical probability distributions. The darker circles are corrected for detection noise and motion blur.

gap distances in Table 1. Already the reduction of the particle-wall-distance by a quarter has led to a doubling of potential energy.

The repulsive forces on the particle in the trap originate from the electrostatic double layer potentials. In a simple picture the interaction energy $W_{PS}(d,h)$ between a charged sphere of radius a and effective surface potential ψ_S and a charged plane with surface potential ψ_P in electrolyte solution with Debye length κ^{-1} can be calculated by:[5]

$$W_{PS}(d,h) = 4\pi\epsilon\epsilon_0 a \psi_{P,eff}\psi_{S,eff}\left(\mathrm{e}^{-(d-h-a)\kappa} + \mathrm{e}^{-(h-a)\kappa}\right), \tag{4}$$

where d is the gap distance and h is the distance of the sphere center from the plane and ϵ and $epsilon_0$ are the vacuum and relative permittivities, respectively. In order to estimate the trapping energy we make a rough simplification and assume that the interaction energy for the particle in the trap is similar to a case where a flat polymer surface is recessed by the trap depth of 10 nm and the particle sits at the slit center ($h = d/2$). Furthermore, we use the same effective surface potential for the polymer surface as for a silicon oxide surface $\psi_{P,0} = -67\,\mathrm{mV}$ ($\psi_{S,eff} = -59\,\mathrm{mV}$),[5] we set the effective surface potential of the particle $\psi_{S,0}$ to the measured zeta potential $\psi_\zeta = -58\,\mathrm{mV}$ ($\psi_{P,eff} = -54\,\mathrm{mV}$) and we use the Debye length $\kappa = 12.5\,\mathrm{nm}$, which was determined by conductivity measurements. The resulting differences in interaction energy ΔW_{edl} are also shown in Table 1. The calculated values are in reasonable agreement for the rough estimation we have done.

The need for motion blur correction becomes obvious when comparing the corrected and uncorrected trapping stiffnesses at a gap distance of $d_{\mathrm{IBM}} \approx 105\,\mathrm{nm}$. The corrected trapping stiffness is reduced by more then 25 %, although the relaxation time $\tau_{\mathrm{rel}} \approx 40\,\mu\mathrm{s}$ and the illumination time $\tau_{\mathrm{illu}} \lesssim 50\,\mu\mathrm{s}$ are almost equal.

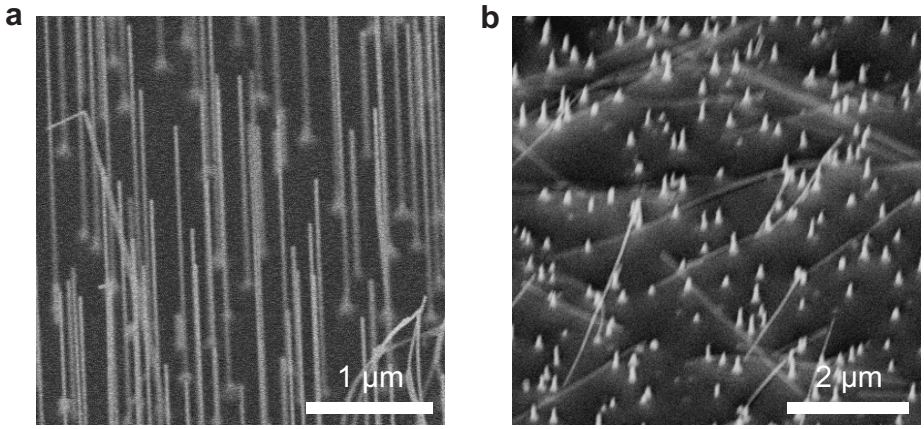

Figure 4: Harvesting of nanowires. (a) SEM image of InAs nanowires grown on a InAs wafer. The wires are approximately 4.3 μm long and have a diameter of $\approx$ 35 nm. The wires are coated with 3 nm Al_2O_3 and 3 nm SiO_2. (b) The nanowires are harvested by shearing a frozen drop of ultrapure water. (a, b) For the imaging the sample was tilted by 45°.

Nanowire harvesting and transport to the target sites

The InAs nanowires were grown epitaxially by using gold seed particles, which act as collectors of vapour-phase precursor materials.[6] The growth was initiated as soon as the precursor gases arsine (AsH_3) and trimethylindium (TMIn) were available at a growth temperature of 430 °C. The wires were also coated with 3 nm Al_2O_3 and 3 nm SiO_2. The high-κ dielectric Al_2O_3 is well suited for gating, yet it has an isoelectric point close to pH $\approx$ 9,[7] which means that the surface does only develop a negative charge in a very basic solution. A second oxide layer (silicon dioxide) was added, which has an isoelectric point around pH $\approx$ 2.[7]

Figure 4 (a) shows an SEM image of the InAs nanowires grown on a (111) InAs substrate with a density of $\approx$ 9 per μm^2. The wires were approximately 4.3 μm long and had a diameter of $\approx$ 35 nm. The wires were harvested by first freezing a drop of ultrapure water (Millipore) on a small substrate piece. The drop was frozen by letting the sample float in a metal dish on liquid nitrogen. Two different methods were used to obtain a final suspension of nanowires. Either the frozen drop was sheared off with tweezers before it started to melt or it was waited until the frozen drop was molten. Some of the wires seem to break during

the freezing or melting due to thermal expansion, since later observation of the not sheared suspension contained nanowires of similar length, yet the concentration was much lower. Figure 4 (b) shows that most of the nanowires are harvested after shearing the frozen drop. For the assembly experiments we harvested the nanowires from $\approx 3 \times 3\,\mathrm{mm}^2$ large samples, which should provide ≈ 80 million nanowires. For stable conditions we typically work with $\geq 20\,\mu$l colloidal suspensions and the suspension has to be confined to gap distances below $d \leq 500\,\mathrm{nm}$, which should result in ≈ 9 nanowires for the entire field of view ($\approx 65 \times 65\,\mu\mathrm{m}^2$). However, due to agglomeration and adsorption to the surfaces we typically observed only around one nanowire at such a confinement.

The nanowire suspension was placed on the patterned sample and confined in the NCA. Figure 5 (a) shows the transport of a nanowire from the left hand side along the yellow dotted trajectory to the electrodes on the right hand side. The insets show images of the same nanowire at different locations (inside the red boxes). First, we determined the contrast of the nanowire by subtracting a background image. Second, the edges of the nanowire in the contrast image were determined by using the Canny edge detection algorithm, which generated a binary image.[8] Third, we performed the Standard Hough Transform on the binary image, which generated a so-called accumulator space of how many points lie on a line with a particular distance to the origin and angle towards the x-axis. Line candidates were determined by local maxima in the parameter space. The ten most dominant peak values, with a minimum line length similar to the length of the nanowire, are depicted by the light blue lines in Figure 5 (a). The average of all detected lines is shown by the dark blue line; this line was used to determine the central position and orientation angle of the nanowire.

The position as well as the orientation of the nanowire were affected by Brownian motion and an electro-osmotic flow. The electro-osmotic flow was generated in either x- or y-direction by applying a square wave-voltage of ± 0.1V 5 Hz on top of a constant voltage of $+0.1$ V. The light blue and light red regions in Figure 5 (b) indicate when these potentials were switched

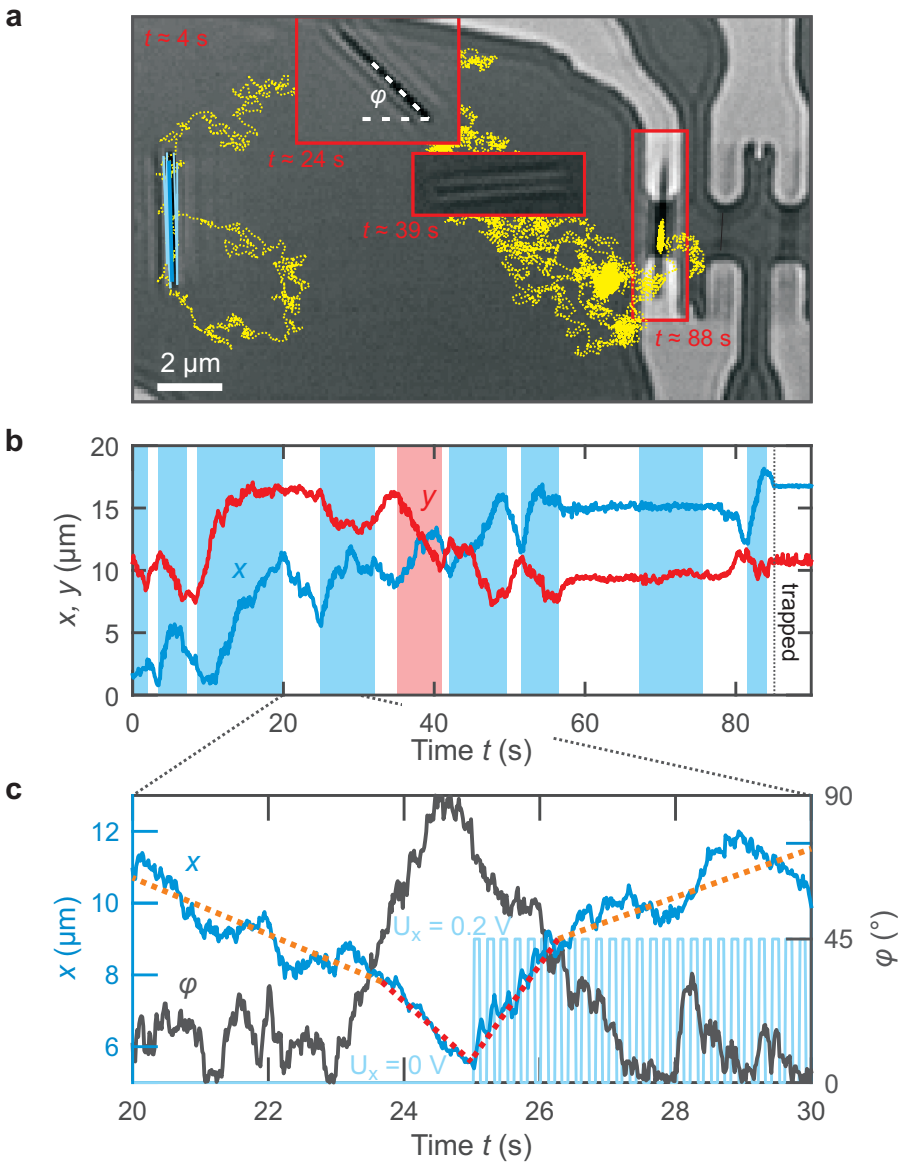

Figure 5: Transport of a nanowire to the trap. (a) Optical images of a nanowire in our NCA. The blue lines depict the detected nanowire position and orientation. The dotted yellow line shows the trajectory of the center of mass of the nanowire and the insets show the nanowire at at a particular time. The wire was trapped after $\gtrsim 85\,\mathrm{s}$ in the PPA groove across two electrodes. (b) The x and y position of the nanowire as a function of time is depicted by the blue and red line, respectively. The nanowire was directed to the trap by applying a square wave-voltage of $\pm 0.1\mathrm{V}$ and $5\,\mathrm{Hz}$ on top of a constant potential $+0.1\,\mathrm{V}$ in either x- or y-direction as indicated by the light blue and light red regions, respectively. (c) The drag on the nanowire depended on its orientation towards the direction of the plug flow. As illustrated by the black line and the slope of the dotted orange/red lines, the more vertical the wire was aligned to the flow direction the larger was the drift of the nanowire. The effective transport was a result of switching the potentials on and off depending on the orientation of the wire.

on. The effective motion of the counter-ions was towards the more negative electrode to compensate the effective potential. This induced a plug flow, which dragged the nanowires in the same direction. After switching the potential off the counter-ions diffused back and dragged the nanowire in the opposite direction. However, the drift of the nanowire was not linear and the net drift was towards the electrodes.

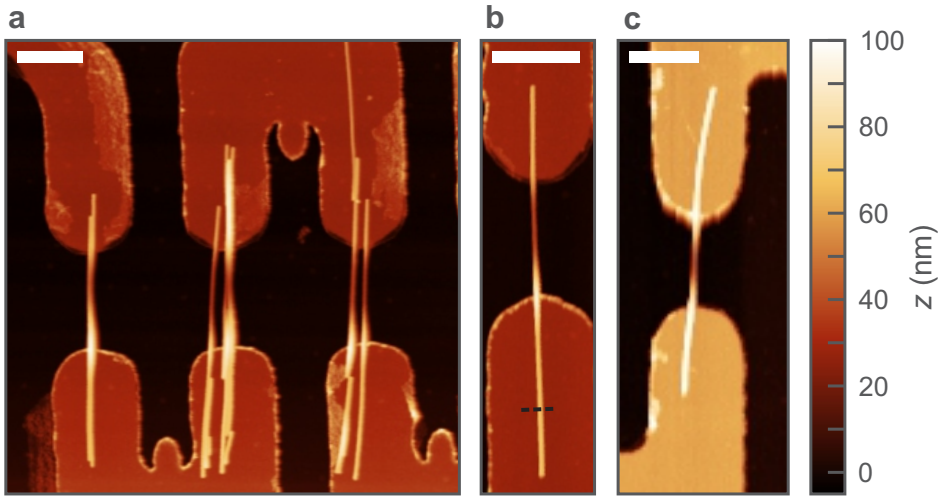

Figure 6: Assembled InAs nanowires. (a - c) AFM image of assembled nanowires after the PPA film was evaporated at $\approx$ 220° C on a hot plate for 10 s. The wires connect two electrodes. In (a) and (b), the electrode thickness is 27 nm and 60 nm in (c). The single nanowires in (b) and (c) have a diameter of $\approx$ 39 nm. (a - f) The scale bars are 1 μm.

We observed an orientation dependent drag of the nanowire, which was stronger if the nanowire was vertically aligned to the flow direction. Figure 5 (c) shows a typical section of the x-position and the angle ϕ between the nanowire and the x-axis. The dotted orange and red lines are guides to the eye. The higher slope of the dotted red lines indicates an increased drift when the nanowire was aligned more vertically ($\phi > 45\,°$), while it was reduced for a more horizontal alignment (dotted orange lines, $\phi < 45\,°$). By selectively switching the electrical field on and off, the particle was transported towards the electrodes. It is important to note that the electric field induced a torque on the polarized nanowire, which tried to align the nanowire parallel to the electric field (flow direction). This force was exploited in dielectrophoretic trapping .[9] However, in our case the applied field strength was $\gtrsim$ 100 times smaller and the Brownian motion dominated the reorientation of the nanowire. By taking

care that the nanowire was in the proximity of a particular polymer groove and by setting the trapping strength with the gap distance, we could select in which groove the nanowire was trapped. The gap distance was reduced from $d \approx 380\,\mathrm{nm}$ to $d \approx 300\,\mathrm{nm}$, during the transport of the nanowire shown in Figure 5.

For completeness, we provide here AFM images of nanowires deposited on 5 assembly sites in Figure 6.

References

(1) Fringes, S.; Skaug, M.; Knoll, A. W. In situ contrast calibration to determine the height of individual diffusing nanoparticles in a tunable confinement. *J. Appl. Phys.* **2016**, *119*, 024303.

(2) Fringes, S.; Holzner, F.; Knoll, A. W. The Nanofluidic Confinement Apparatus: Studying confinement dependent nanoparticle behavior and diffusion. *Beilstein J. Nanotechnol.* **2018**, *9*, 301–310.

(3) Skaug, M. J.; Schwemmer, C.; Fringes, S.; Rawlings, C. D.; Knoll, A. W. Nanofluidic rocking Brownian motors. *Science* **2018**, *359*, 1505–1508.

(4) Wong, W. P.; Halvorsen, K. The effect of integration time on fluctuation measurements: calibrating an optical trap in the presence of motion blur. *Opt. Express* **2006**, *14*, 12517–12531.

(5) Behrens, S. H.; Grier, D. G. The charge of glass and silica surfaces. *J. Chem. Phys* **2001**, *115*, 6716.

(6) Dick, K. A.; Deppert, K.; Samuelson, L.; Seifert, W. InAs nanowires grown by MOVPE. *J. Cryst. Growth* **2007**, *298*, 631–634.

(7) Parks, G. A. The isoelectric points of solid oxides, solid hydroxides, and aqueous hydroxo complex systems. *Chem. Rev.* **1965**, *65*, 177–198.

(8) Canny, J. A computational approach to edge detection. *IEEE Trans. Pattern Anal. Mach. Intell.* **1986**, 679–698.

(9) Freer, E. M.; Grachev, O.; Duan, X.; Martin, S.; Stumbo, D. P. High-yield self-limiting single-nanowire assembly with dielectrophoresis. *Nat. Nano* **2010**, *5*, 525–530.